An invisible-stylus-based coordinate measurement system via scaled orthographic projection☆

Joshua A. Gordon[a,*], Steven S. Borenstein[b]

[a] Communications Technology Laboratory, National Institute of Standards and Technology, Boulder, CO 80305, United States
[b] Integrated Remote and In Situ Sensing, University of Colorado, Boulder, CO 80309, United States

ABSTRACT

We present on a simple yet effective method for creating an invisible stylus from which a non-contact 3-D coordinated measuring system (the PiCMS) is realized. This invisible stylus dubbed a Pixel Probe is created through the orthographic projection of a spherical mounted reflector (SMR) through a trifocal camera system. Through this, a single point in space that is linked to a laser tracker world frame is mapped to a unique set of pixel coordinates in the trifocal camera creating the Pixel Probe. The system is constructed through the union of a Pixel Probe, a laser tracker, and calibrated XYZ stage, and does not require contact to obtain a measurement. In the current configuration, system resolution and accuracy better than $20\,\mu m$ is demonstrated on objects in the meso/micro scale that are well below the range of a laser tracker alone. A simple single-point coincidence condition allows the user to specify a measurement coordinate by pointing-and-clicking in the images captured by the Pixel Probe. We describe this system using multi-view geometry vision theory and present proof of concept measurement examples of 2-D and 3-D objects.

1. Introduction: Pixel Probe non-contact CMS

Many types of coordinate measurement systems (CMS) exist ranging from facility type coordinate measuring machines (CMM) [1–3], to portable systems [4,5]. The range of capability of these systems can be extended through the myriad probes available including touch trigger probes [1,6] and impressively sensitive and elegant tactile probes [7–9]. Each system has strengths and weaknesses, limitations and uncertainties associated with the way in which they capture and measure a coordinate. As such, having a variety of options at hand enhances the metrologist ability to make meaningful measurements.

A variety of contact and non-contact probes have been devised to sense coordinates in 3-D. Contact stylus-based probes provide perhaps the most direct method for measuring coordinates and range from millimeter sized ball types as in touch-trigger probes [1,6] to micron sized tactile optical fibers [7]. Contact based systems can provide some of the most accurate measurements in the world and variations are used to establish traceability at national metrology institutes [3]. However, these systems are less well suited for measuring larger surfaces and may not be portable. Non-contact methods such as photogrammetry [4,5], laser line scanners [10,11], structured light [12], and laser radar [4] provide efficient means for capturing data over large surfaces of many

m^2 yet may not be well suited for measuring micro or meso scaled objects nor be as accurate or repeatable as contact based methods. Furthermore, some systems such as laser trackers [13,14] and photogrammetry [5] are most accurate when optimized to measure specifically designed targets such as the spherical-mounted reflector (SMR) [13,15] (as for a laser tracker) and point targets [5] (as for photogrammetry) rather than make direct coordinate measurements on objects.

Here we present a proof of concept on a different type of CMS that parallels stylus based systems yet does not require contact and also leverages optical and machine vision elements yet is *not* a photogrammetry system and may be in some sense considered a hybrid system. This system in essence produces an invisible stylus non-contact probe from which a CMS is constructed by uniting it with a portable laser tracker and calibrated XYZ stage. The laser tracker provides a means for determining the probe location in 3-D and the XYZ stage allows a user to efficiently target and position the probe on a coordinate to be measured. Because this CMS works inherently with a laser tracker, measurements live in the world coordinate system W of the laser tracker, and thus can be linked to other laser tracker measurements, thereby bridging portable and non-portable metrology.

Only a conceptual description of the invisible stylus dubbed a Pixel

---

Probe was reported on in Refs. [16,17]. In this manuscript we develop a more rigorous theoretical model of the Pixel Probe, and then through this model, extend its functionality to a CMS configuration which we call the PiCMS. The Pixel Probe and PiCMS are developed using multi-view geometry vision theory [18] and necessary calibration steps and system design details are given. This manuscript has three main parts: Section 2 develops the Pixel Probe which by itself can be used to make measurements, Section 3 develops the PiCMS which improves the usability and convenience of the Pixel Probe and in Section 4 we present proof of concept measurements. Appendix A provides further details on extrinsic calibration and camera pose estimation required for the PiCMS.

2. Pixel Probe

2.1. Description

A useful visualization for the Pixel Probe is that of a system of specifically calibrated cameras whose function is to project a set of image coordinates to a *single* point in space $\mathbf{X}^*$. Furthermore, in this concept, the location of $\mathbf{X}^*$ is tracked in the world frame W of a coordinate measurement system such as a laser tracker. One can imagine a pixel floating in space that is able to be tracked by a laser tracker or similar system. The 2-D image coordinate $\mathbf{x}_{img} = [x_{img}, y_{img}]^T$ this pixel appears at in the camera system has a direct correspondence to only one 3-D coordinate $\mathbf{X}^* = [X^*, Y^*, Z^*]^T$ in W. This concept is illustrated in Fig. 1.

As opposed to stereo vision or multi-view photogrammetry [4,5,18] systems where full frame images are correlated to reconstruct coordinate measurements across a field of view, only the single point $\mathbf{X}^*$ is used here. Furthermore, the camera system does not form a 2-D or 3-D reconstruction of a scene, nor does it track any targets as is common in photogrammetry. As such, although cameras are used, the Pixel Probe does not function as a photogrammetry system and is distinctly different. Rather it provides a direct and repeatable measurement at a single 3-D coordinate. Below, we elaborate on this distinction as well as

the use of scaled orthographic projection as a means of realizing the Pixel Probe using cameras.

The point $\mathbf{X}^*$ acts as an invisible stylus so that non-contact measurements can be made at a specific and repeatable location with a laser tracker to approximately the resolution of a single pixel (which is on the order of microns). This is about 10^4 smaller than a typical SMR (38.1 mm diameter) laser tracker target and about 10^3 smaller than the width of the laser beam used by the laser tracker. The Pixel Probe in comparison has a much smaller spatial scale than an SMR and therefore extends the size range of objects that can be measured with a laser tracker alone, down to the meso/microscale (approx. 50 mm-to-1 μm) [19] well below the typical macroscale/meso (approx. > 1 m-to-50 mm) of a laser tracker.

2.2. Pixel Probe multi-view geometry

Given a laser tracker whose native coordinate system is defined as the world frame W, the first step in realizing the Pixel Probe is to establish a local coordinate system L^* within W that is measurable by the laser tracker. All measurements ultimately reside in W which defines the coordinate metrology space of the PiCMS. Both W and L^* define 3-D space (IR^3). Within L^* resides a fixed camera system which projects a set of 2-D (image space) [20] coordinates from IR^2 onto *one* (object space) IR^3 coordinate $\mathbf{X}^* = [X^*, Y^*, Z^*]^T$. Here, a trifocal imager [18] embodiment is used for the camera system and consists of three separate cameras constructed from three imaging lenses paired with three imaging arrays (i.e., CMOS, CCD). Cameras are represented using the pinhole model [18]. The three cameras are nominally arranged in a tetrahedral configuration with the optical axis of each camera coincident with a side of the tetrahedral so that all three optical axes nominally intersect at the vertex and the field of view of each camera overlap as shown in Fig. 2.

This configuration is chosen in order to minimize ambiguity when projecting points from each camera in IR^2 back to a single point in IR^3 within L^*. Each camera is specified by an intrinsic coordinate system with origins at camera centers C_1, C_2, & C_3, respectively all which reside in L^*. The action of the jth camera, is a mapping between points $\mathbf{X}$ in IR^3, to points $\mathbf{x}_j$ in IR^2 at the image plane of camera C_j. The mapping [18]
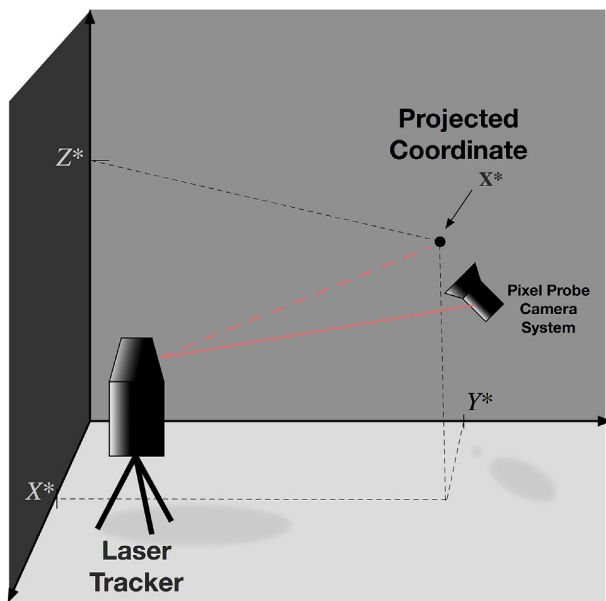

Fig. 1. Pixel Probe concept. A laser tracker measures the Pixel Probe camera system. The red solid line represents the measurement laser beam. The Pixel Probe camera system projects a set of pixels to only the *single* coordinate $\mathbf{X}^* = [X^*, Y^*, Z^*]^T$. Through the Pixel Probe the laser tracker sees a measurement at $\mathbf{X}^*$ (represented by the dotted red line) in the World coordinate system W. (For interpretation of the references to color in this figure legend, the reader is referred to the Web version of this article.)
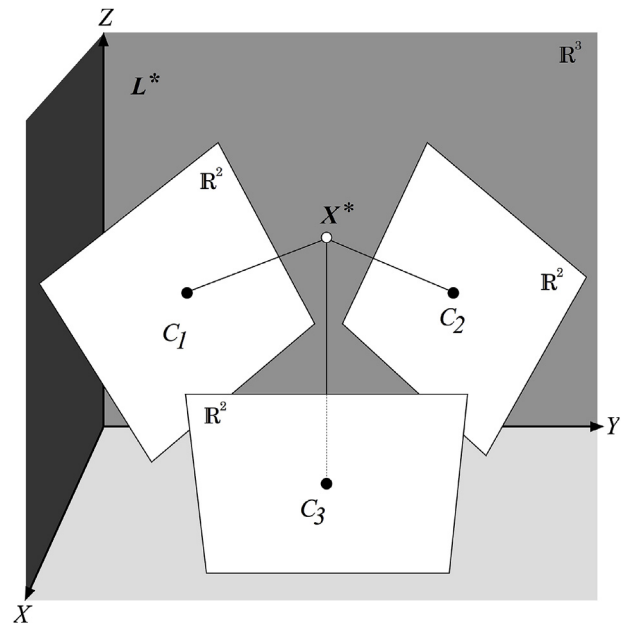

Fig. 2. The trifocal imager used to develop the Pixel Probe and PiCMS. Three cameras defined by centers C_1, C_2, & C_3 are arranged in a tetrahedral configuration having fixed poses in local coordinate system L^*. Camera image planes define IR^2 and L^* defines IR^3. The three image axes intersect at point X^*.

represented by the 3 × 4 camera projection matrix $[P_j]$, is

$$\mathbf{x}_j = [P_j]\mathbf{X} \qquad (1)$$

With,

$$[P_j] = [K_j][R_j|\mathbf{t}_j] \qquad (2)$$

where $[K_j]$ is the camera calibration matrix containing the focal length and image distortion coefficients. $[R_j]$ is the 3 × 3 rotation matrix and $\mathbf{t}_j$ the translation vector from the origin of a reference coordinate system. Together $[R_j]$ and $\mathbf{t}_j$ describe the pose of camera C_j. The $[P_j]$'s are the basic building blocks from which the Pixel Probe and PiCMS are developed.

2.3. Pixel Probe calibration

We distinguish two levels of calibration for the Pixel Probe: camera calibration, and Pixel Probe calibration. An intrinsic calibration method is used to determine the camera distortion through $[K_j]$ for each camera. As this is a well-documented process [18] with many methods available we leave the choice up to the reader. For the remainder of the paper we assume $[K_j]$ are known and the cameras are intrinsically calibrated.

2.3.1. Orthographic projection of SMR

The second calibration is used to define the Pixel Probe and provides a means to realize the point $\mathbf{X}^*$ in such a way that it can be tracked and measured with a laser tracker thus creating the invisible stylus. This is achieved through the scaled orthographic projection [18,21] of an SMR laser tracker target. Laser tracker target SMRs (see Fig. 3) are constructed from a hollow corner cube reflector made from three orthogonal mirrors mounted in a hardened steel spherical housing. Such SMRs typically come in two sizes, 38.1 mm and 12.7 mm diameter and are commonly referred to (as we will do throughout this paper) in English units as 1.5″ and 0.5″, respectively. Before moving on, the traits of commercially available laser tracker target SMRs are worth noting: 1) The spherical hardened steel housings have tolerances on sphericity routinely ≤ 3 μm [13], and 2) The offset between the center of the spherical housing and the center of the corner cube reflector it encases are routinely within ≤ 3 μm [13]. Thus by design, the geometrical center of an SMR is co-located with the coordinate measured with a laser tracker.

In calibrating the Pixel Probe we make use of these traits along with considering the image projection of the SMR through the cameras in the following scenario … An SMR is placed with its center nominally at the vertex of the trifocal imager so that it is near the optical axis of each camera and also several focal lengths away. The aperture of the SMR is pointed away from camera C_j so that only the solid steel back hemisphere of the SMR is viewed through the cameras. Focus is set on the center of the SMR. Given the size of the SMR, the assumed intrinsically calibrated camera (e.g. negligible distortion) and the distance the SMR is from the camera, the formation of the image of the SMR can be
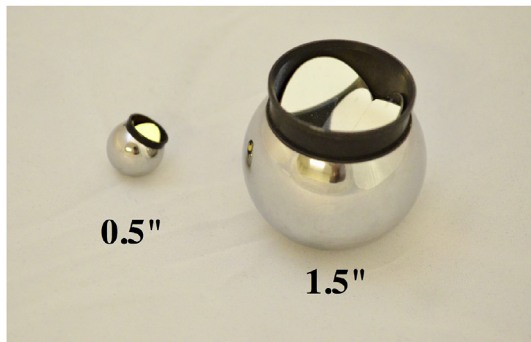

Fig. 3. 0.5″ and 1.5″ spherically-mounted-reflector (SMR) laser tracker targets.
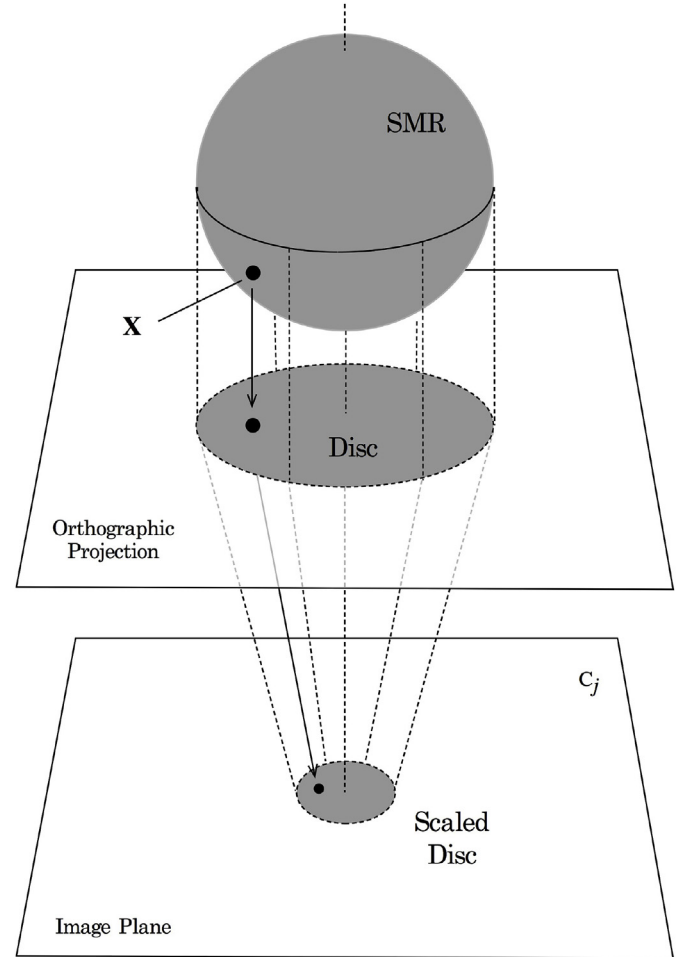

Fig. 4. Scaled orthographic projection of an SMR through camera C_j. The 3-D coordinates $\mathbf{X}$ (black dot) on the SMR sphere are mapped to a plane through orthographic projection creating a disc. Parallel dotted lines depict the mapping progression from 3-D to 2-D. The disc is scaled by the camera onto the image plane while preserving the 2-D coordinate relationships.

considered a weak perspective projection and thus treated as a scaled orthographic projection [18,21].

Under scaled orthographic projection the mapping of a point in IR^3 to IR^2 along the direction of the optical axis and perpendicular to the image plane is represented by the projection matrix,

$$[P_{orth}] = \begin{bmatrix} \$ & 0 & 0 & 0 \\ 0 & \$ & 0 & 0 \\ 0 & 0 & 0 & 1 \end{bmatrix} \qquad (3)$$

The result of this projection is that the Z-coordinate is stripped away for points on the SMR sphere $\mathbf{X}_s = [X_s, Y_s, Z_s, 1]^T$, leaving the X and Y coordinates at the image plane scaled by a factor $\$$ that is governed by the camera magnification. So that, $\mathbf{X}_s \rightarrow \mathbf{x}_{orth} = [\$X_s, \$Y_s, 1]^T$ via,

$$\begin{bmatrix} \$X_s \\ \$Y_s \\ 1 \end{bmatrix} = \begin{bmatrix} \$ & 0 & 0 & 0 \\ 0 & \$ & 0 & 0 \\ 0 & 0 & 0 & 1 \end{bmatrix} \begin{bmatrix} X_s \\ Y_s \\ Z_s \\ 1 \end{bmatrix} \qquad (4)$$

This projection can be thought of as a straight orthographic projection followed by a linear scaling onto the image plane of the camera. This is depicted in Fig. 4. The result is that the image of the three dimensional spherical SMR becomes that of a disc with a radius that of the SMR scaled by $\$$. Although this may seem intuitive under visual perception, weak perspective projection through a camera system is in general not guaranteed and thus neither is representation as
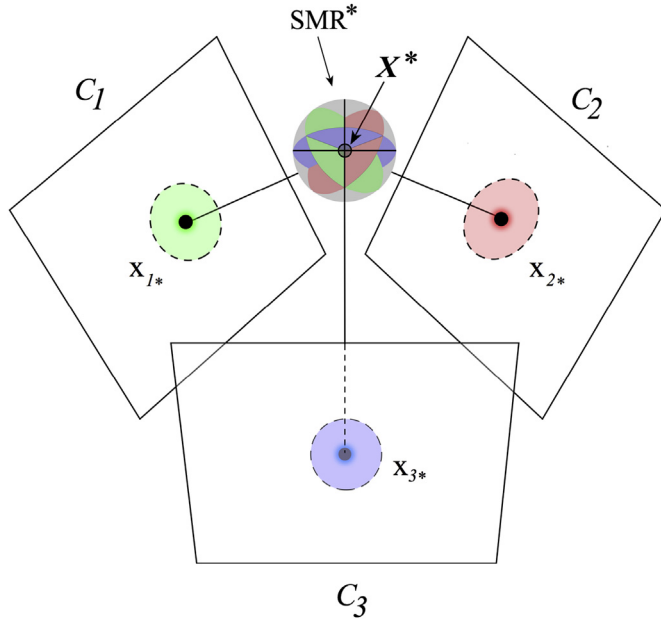
Fig. 5. Scaled orthographic projection of SMR^* onto the image planes of cameras C_1, C_2, & C_3. The projected orthographic discs are represented as dotted outlines on each camera plane. Conjugate pairs of discs at the image planes and cross-sectional planes at SMR^* are color coded for each camera. The disc centroid coordinates $\mathbf{x}_{1*}$, $\mathbf{x}_{2*}$, & $\mathbf{x}_{3*}$ conjugate to $\mathbf{X}^*$ define the Pixel Probe. (For interpretation of the references to color in this figure legend, the reader is referred to the Web version of this article.)

orthographic projection. As such, some amount of care must be taken to ensure the correct projection of the SMR is achieved by the camera system.

The projection of the disc at the image plane is conjugate to the cross-sectional plane of the SMR that passes through its center. Including the projections from all three cameras results in three planes intersecting at the center of the SMR (see Fig. 5). Furthermore, the centroids of the three orthographic discs defined as $\mathbf{x}_{1*}$, $\mathbf{x}_{2*}$, $\mathbf{x}_{3*}$ for cameras C_1, C_2, C_3 respectively are conjugate to the center coordinate $\mathbf{X}^*$ of the SMR in IR^3. These centroids have unique coordinates in the pixel array of each camera (in general not necessarily at the center of a pixel), and define the Pixel Probe.

$$\mathbf{x}_{1*} = \begin{bmatrix} x_{1*} \\ y_{1*} \end{bmatrix}, \quad \mathbf{x}_{2*} = \begin{bmatrix} x_{2*} \\ y_{2*} \end{bmatrix}, \quad \mathbf{x}_{3*} = \begin{bmatrix} x_{3*} \\ y_{3*} \end{bmatrix} \tag{5}$$

2.3.2. Brightfield imaging of SMR

A bright field imaging scheme is used to isolate the orthographic disc and to actualize $\mathbf{x}_{1*}$, $\mathbf{x}_{2*}$, $\mathbf{x}_{3*}$. For this, a 0.5″ diameter SMR was placed at the vertex of the trifocal imager denoted SMR^*, as in Fig. 5. This diameter SMR was found to work well with the field of view of typical machine vision cameras and lenses in the focal length range of 12 mm–35 mm. A conical kinematic magnetic nest mounted to a 0.5″ diameter optical post was used to hold SMR^* while also maximizing the observable perimeter of its silhouette in each camera.

With SMR^* in place, a planar Lambertian [22] white light source is place behind it, diametrically opposite from one of the cameras C_j. This is shown in Fig. 6. A white-light LED panel with a diffuser was used here as the Lambertian source. The SMR aperture is pointed away from the camera so that the solid hemisphere is viewed and the source is placed far enough away such that illumination on SMR^* is uniform and not dependent on minor alignment changes relative to the camera optical axis. This is easily verified by viewing the SMR in the images while moving the light source. More sophisticated sources such as telecentric illuminators [23] could also be used if available. To eliminate stray
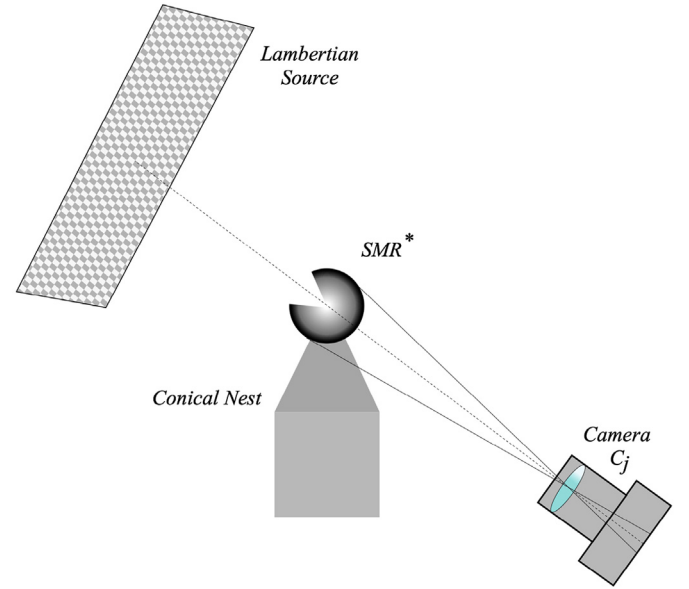

Fig. 6. The bright field illumination scheme used for calibrating the Pixel Probe. SMR^* is held in the conical nest and illuminated diametrically opposite camera C_j by the Lambertian source. The aperture of the SMR is pointed away from the camera so only the spherical form is imaged.

light an absorbing shroud made of black flocking can be used to cover the setup. Gamma adjustment in the images is also useful for improving edge definition and compressing image values during this process. A camera image showing the orthographic projected disc resulting from this illumination scheme is shown in Fig. 7.

The image observed in the camera is that of the orthographic projected disc of the SMR^* on top of the silhouette of the conical nest. The disc is well defined and surrounded by a uniform intensity. Because of the cone-style nest, nearly 320° of the disc are observed.

From this bright field image, the coordinate $\mathbf{x}_{j*}$ for the centroid of the disc in camera C_j is found using a machine vision algorithm. A semi-
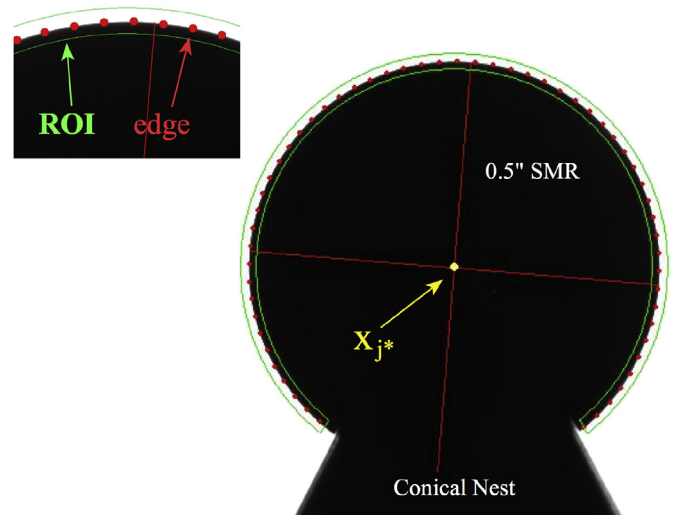
Fig. 7. The scaled orthographic projected disc of a 0.5″ SMR held by conical nest. Determination of $\mathbf{x}_{j*}$ image conjugates are achieved through the edge finding algorithm and circle fitting. Conjugate $\mathbf{x}_{j*}$ (yellow dot) is determined by applying the edge finding algorithm in the image from camera C_j. Red crosshairs show the major and minor axes of the fit ellipse. A closeup (Top Left) shows the ROI (green) bounding the disc and edge points (red). (For interpretation of the references to color in this figure legend, the reader is referred to the Web version of this article.)

annular region of interest (ROI) is established around the perimeter of SMR^*. This shaped ROI allows the silhouette of the conical nest to be excluded by choosing the start and stop angle of the semi-annulus. The inner radius and outer radius of the semi-annulus are chosen to bound the edge of the orthographic disc. An edge finding algorithm is then used to identify the edge of the disc by detecting the sharp dark-to-light transition along radial trajectories every 2° between the inner and outer edge of the ROI. The ROI and edge detection process are also shown in Fig. 7. As the centroid coordinate of the disc does not depend on its area or knowing accurate dimensions, the requirement for the edge detection algorithm having to determine dimensions with accuracy can thus be relaxed (with the caveat that the illumination be uniform). In other words, an over or under estimation of the diameter of the image of SMR^* will not change the found centroid location $\mathbf{x}_{j*}$. Sensitivity to image errors could be minimized further by the use of appropriate object-space-telecentric imaging lenses [20,23]. In this case the centroids will be significantly less sensitive to accidental variations in magnification while achieving focus. However, such lenses can become very large and impracticable due the path of the chief ray for appreciable fields of view.

As the $\mathbf{x}_{j*}$ are based on the direct measurement of SMR^* disc, they are obtained with sub-pixel resolution. The centroid finding process is repeated for the other two cameras so that all three centroids $\mathbf{x}_{1*}$, $\mathbf{x}_{2*}$, $\mathbf{x}_{3*}$ are established and *stored in memory*.

2.3.3. Linking to laser tracker

The last step in calibrating the Pixel Probe is to link $\mathbf{X}^*$ to the laser tracker by establishing the local coordinate system L^* within which $\mathbf{X}^*$ uniquely resides. There are many possible ways to achieve this. However, a straight forward method, and one that also nicely depicts the actualization of the Pixel Probe, is to mount a set of SMRs, $\{SMR_1 : SMR_j\}$ at varying heights and locations on the mechanical base the cameras are fixed to. We describe this method first then adopt variations of it later on. Shown in Fig. 8 is a Pixel Probe system that has the cameras along with the set $\{SMR_1 : SMR_5\}$ fixed to a small optical breadboard.

To link $\mathbf{X}^*$, SMR^* as well as the $\{SMR_1 : SMR_5\}$ are measured with the laser tracker thereby creating a constellation of six points in W
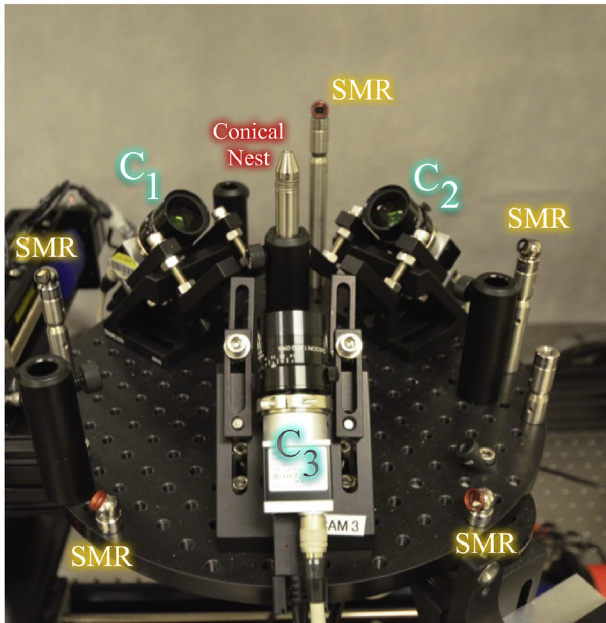

Fig. 8. The Pixel Probe construction used in the PiCMS. Three identical 5 MP CMOS cameras having $2.2\,\mu m$ sized pixels and configured with 18 mm focal length lens are labeled C_1, C_2, & C_3 and shown along with the SMRs and conical nest.

representing the center coordinates of the SMRs. This constellation simultaneously defines both L^* and $\mathbf{X}^*$. We note in particular that (with mechanical rigidity assumed), $\mathbf{X}^*$ has a fixed relationship to $\{SMR_1 : SMR_5\}$ *regardless of SMR^* being physically there*. Thus the actualization of the Pixel Probe is completed by *removing SMR^** leaving behind the projected image of $\mathbf{X}^*$ via $\mathbf{x}_{1*}$, $\mathbf{x}_{2*}$, $\mathbf{x}_{3*}$ that were stored in memory and realize that to retrieve the location of $\mathbf{X}^*$ within L^* we need only re-measure $\{SMR_1 : SMR_5\}$ with the laser tracker. As only three out of $\{SMR_1 : SMR_5\}$ are necessary to define L^* here five SMRs were used in order to reduce errors due to noise, computational precision, and the finite accuracy of the laser tracker.

Through this calibration, $\mathbf{X}^*$ achieves a direct correspondence between the laser tracker and any coordinate within W that gets imaged by the trifocal imager. Next, we consider making coordinate measurements with the Pixel Probe for an object placed in the focal volume of the trifocal imager.

2.4. Coordinate measurements

Because the Pixel Probe is intrinsically linked to a laser tracker it can be used to make measurements by itself. The IR^3 coordinate $\mathbf{X}_{obj}$ of a feature on an object in W maps to three coordinates of the trifocal imager in IR^2 as,

$$\mathbf{x}_{1,obj} = \begin{bmatrix} x_{1,obj} \\ y_{1,obj} \end{bmatrix}, \quad \mathbf{x}_{2,obj} = \begin{bmatrix} x_{2,obj} \\ y_{2,obj} \end{bmatrix}, \quad \mathbf{x}_{3,obj} = \begin{bmatrix} x_{3,obj} \\ y_{3,obj} \end{bmatrix} \quad (6)$$

The coordinate measurement of $\mathbf{X}_{obj}$ in IR^3 is simply obtained by orienting the Pixel Probe such that $\{\mathbf{x}_{1,obj}, \mathbf{x}_{2,obj}, \mathbf{x}_{3,obj}\}$ coincides with $\{\mathbf{x}_{1*}, \mathbf{x}_{2*}, \mathbf{x}_{3*}\}$. Letting $\delta_j = \|\mathbf{x}_{j,obj} - \mathbf{x}_{j*}\|$, and $\Delta = \|\mathbf{X}_{obj} - \mathbf{X}^*\|$, this coincidence relation in IR^2 is,

$$\sum_{j=1}^{3} \delta_j = 0 \quad (7)$$

which simultaneously satisfies the desired condition in IR^3,

$$\Delta = \|\mathbf{X}_{obj} - \mathbf{X}^*\| = 0 \quad (8)$$

and makes $\mathbf{X}_{obj}$ coincident with $\mathbf{X}^*$ in W. Capturing $\{SMR_1 : SMR_5\}$ with the laser tracker under this condition completes the measurement and we obtain $\mathbf{X}_{obj}$ within W without physical contact.

2.5. Modes of operation

In some sense, the Pixel Probe achieves the function of a nearly infinitesimal invisible stylus located at $\mathbf{X}^*$ yet it has other aspects that further enhance its utility for coordinate measurements and spatial metrology. As a stylus it provides a very repeatable and unambiguous point measurement free from re-projection and correlation errors that can result from relying on 3-D reconstruction using full image frames. This is mainly due to the direct calibration achieved using the orthographic projection of the SMR as described above. As such, rather than determining coordinates in IR^3 through a parallax disparity requiring calibration across entire sets of images, we have reduced the measurement to a single well known point, i.e. $\mathbf{X}^*$ and link this to a laser tracker. Therefore, unambiguous, precises and quite accurate knowledge (as demonstrated below) of a single point is traded for full 3-D reconstruction across an image that is less accurate and limited by some of the challenges in full frame multi-view camera calibration. This single-point function is utilized in two main modes of operation, "Direct Mode" and "Feature Mode". These modes allow different types of measurements to be obtained with a laser tracker and leverage both the stylus-like nature and imaging nature of the Pixel Probe.

2.5.1. Direct Mode

In Direct Mode, the Pixel Probe functions like a stylus and obtains a single point measurement through the one-to-one correspondence
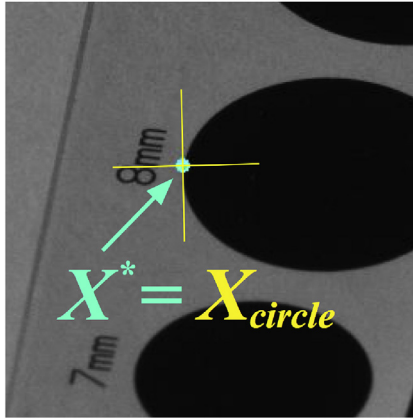
Fig. 9. Direct Mode of operation using the optical shape target. Image is shown from one of the cameras. The Pixel Probe is defined by $\mathbf{X}^*$ (center of blue dot), and is coincident with a location $\mathbf{X}_{circle}$ at the edge of the 8 mm diameter circle (center of yellow cross-hairs). (For interpretation of the references to color in this figure legend, the reader is referred to the Web version of this article.)

between $\mathbf{X}^*$ and the coordinate $\mathbf{X}_{obj}$ of a physical feature on an object via (7) & (8). A canonical example of this is shown in Fig. 9 where a point on the edge of a planar circular optical target is measured.

The Pixel Probe is represented by the blue dot (with coordinates $\mathbf{x}_{1*}$, $\mathbf{x}_{2*}$, $\mathbf{x}_{3*}$) in the image captured from one of the cameras (note that the size of the blue dot has been exaggerated for visibility in the figures and represents a single point coordinate at its center). When the center of the blue dot is placed at a location on the edge of the circle so that $\mathbf{X}_{obj} = \mathbf{X}_{circle}$, then $\mathbf{X}^*$ is also at the same time physically at the corresponding location in IR^3. The laser tracker captures the set $\{SMR_1: SMR_5\}$, and subsequently, $\mathbf{X}_{circle}$ in the laser tracker world frame W is obtained. Moving the Pixel Probe about the circumference of the circle and continuing this process aligning $\mathbf{X}^*$ with different locations generates a set of points which can then be fit to obtain not only circle dimensions (perimeter, and radius) but *full pose* within W (center coordinate, and normal vector).

2.5.2. Feature Mode

In Feature Mode image processing is used for identifying features from the scene observed by the Pixel Probe. Unlike in photogrammetry systems, no reconstruction from image space-to-object space is used. To the Pixel Probe, features that have been extracted at the camera image planes have a conjugate in W. As such these features represent structures in 3-D space that need not have a literal corresponding form. These structures may be derived from any number of means (optical filters, artificial intelligence, machine vision algorithms, etc.) able to identify patterns of interest in the images. Furthermore, these structures may be microns in size and need only be resolvable by the cameras to be measured. As such, scaling camera resolution and magnification can very easily enhance the resolution and spatial scale measurable with the Pixel Probe.

Through the mapping of $\mathbf{X}^*$ to W, the Pixel Probe provides a means to measure coordinates of these derived structures with a laser tracker. We demonstrate this again with the canonical example of the circle target. In Direct Mode, finding the center of the circle in W required measuring individual points about the perimeter, then fitting a circle to these points from which the center can be determined. Alternatively, image processing can be applied to the images to first identify (not measure) the center of the circle. Due to normal perspective distortion the circle appears as an ellipse. Thus, by applying an ellipse identifying filter comprised of an ROI and an edge finding algorithm, the circle center $\mathbf{X}_{cc}$ can be identified and prescribed a pixel coordinate $\mathbf{x}_{j,cc}$ within the images. With $\mathbf{X}_{cc} = \mathbf{X}_{obj}$, initially, the coincidence condition (8) is in general not satisfied such that $\mathbf{x}_{j,cc}$ appear away from $\mathbf{x}_{j*}$ in the
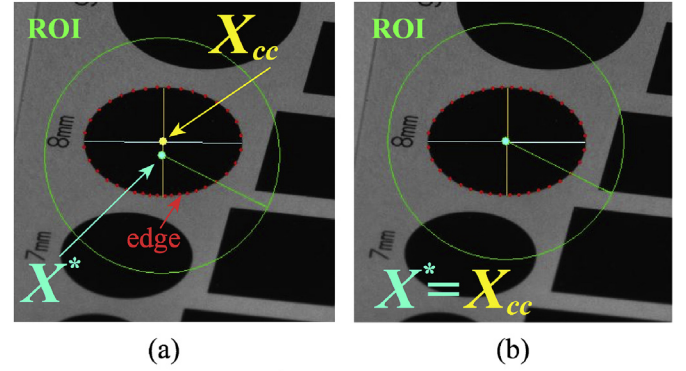
Fig. 10. Feature Mode of operation using the 8 mm diameter circle of the optical shape target. Images are shown from one of the cameras. Circles appear as ellipses due to normal perspective distortion. **(a)** First the center of the circle, $\mathbf{X}_{cc}$ is found using the edge detection image filter. The ROI (green boundary), edge points (red dots) and major and minor ellipse axes (yellow cross-hairs) are shown. The Pixel Probe is defined by $\mathbf{X}^*$ (center of blue dot), and at first is not coincident with the found circle center $\mathbf{X}_{cc}$ (center of yellow dot). **(b)** After positioning the Pixel Probe the coincidence condition is satisfied with $\mathbf{X}^* = \mathbf{X}_{cc}$ and the coordinate of the circle center is able to be measured with the laser tracker. (For interpretation of the references to color in this figure legend, the reader is referred to the Web version of this article.)

images. This is shown in Fig. 10 (*a*), where the location of $\mathbf{x}_{j,cc}$ corresponding to $\mathbf{X}_{cc}$ is shown as a yellow dot, and the location of $\mathbf{x}_{j*}$ corresponding to $\mathbf{X}^*$ is shown as a blue dot (note again the dot sizes are exaggeration). The Pixel Probe is then moved such that $\mathbf{X}^*$ is coincident with $\mathbf{X}_{cc}$ thus, satisfying (8) as shown in Fig. 10(*b*). The laser tracker then captures $\{SMR_1: SMR_5\}$ once again obtaining $\mathbf{X}_{cc}$ in W. Therefore in Feature Mode $\mathbf{X}_{cc}$ is obtained through measuring the coordinate of the center of the circular pattern as identified with the image filter and not by deliberately measuring the shape of the circle.

3. Non-contact CMS (PiCMS)

The usability and convenience of the Pixel Probe can be improved by extending it to CMS configuration (called PiCMS). For this the Pixel Probe is attached to a motorized three-axis (X, Y, Z) translation stage having machine coordinate M (See Fig. 11). An extrinsic calibration described in Appendix A is used to estimate the location of $\mathbf{X}^*$ within M so that the XYZ stage can autonomously perform the movement required to satisfy coincidence relations (7) and (8). Since W intrinsically follows the laser tracker, $\mathbf{X}^*$ is always tracked correctly regardless of where the laser tracker is placed. Thus, by design the extrinsic calibration also allows for the laser tracker to be relocated if need be without loss of calibration so that it is not tied up indefinitely and can be pulled in and out of the system for other use. The hierarchy of frames (World-to-cameras) used to describe the PiCMS is $W \rightarrow M \rightarrow L^* \rightarrow C_1 \rightarrow C_2 \rightarrow C_3$. This is depicted in Fig. 12.

3.1. PiCMS design

The Pixel Probe used here was constructed from three low distortion machine vision lenses and 5 mega pixel monochrome CMOS sensors. Lenses used were also "high-G" lenses and are capable of handling high G-forces, vibration due to motion, and changes in orientation without image shifts. This is an important design consideration as the alignment of image coordinates that results from the orthographic projection of the SMR are quite sensitive to even minor lens shifts. Lens focal lengths are 18 mm and set to F/5.6 and sensor pixel size is 2.2 μm. The working distance from the lenses to $\mathbf{X}^*$ was set to give a magnification of approximately 10× (image-to-object space) and a pixel foot print of $\approx 22\,\mu$m at $\mathbf{X}^*$. Manufacturer stated distortion values of 0.01% are
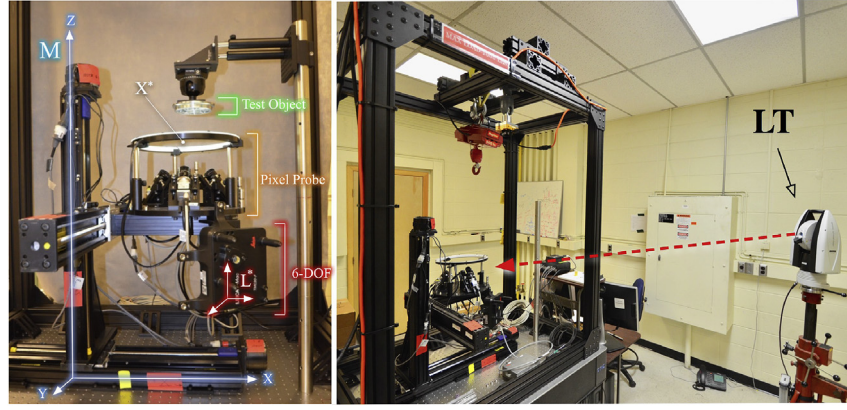
Fig. 11. Construction elements of the PiCMS. (Left) Colored labels identify: (orange) Pixel Probe with ring light, (white) location of $\mathbf{X}^*$, (blue) XYZ stage and corresponding machine frame M, (red) 6-DOF laser tracker target and corresponding local frame L^*. (Right) Complete system with laser tracker (**LT**), red dotted line depicts the laser beam path. (For interpretation of the references to color in this figure legend, the reader is referred to the Web version of this article.)
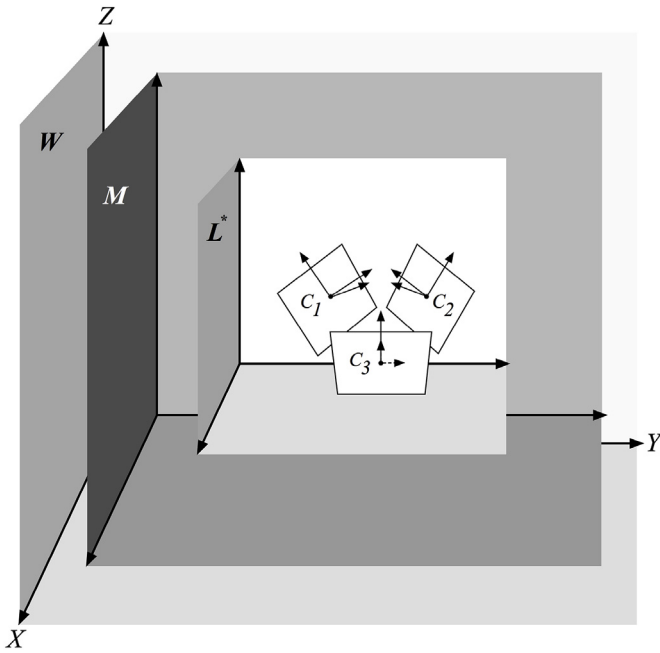
Fig. 12. The hierarchy of coordinate frames: World (W), Machine (M), Local (L^*), Cameras (C_j) used to describe the PiCMS. Frames W, M, L^* are shown oriented similarly for clarity but can be posed arbitrarily.

consistent with the values found in $[K_j]$. The cameras were mounted on a 0.5″ thick solid aluminum optical bread board. A ring light was fixed above the Pixel Probe which could be configured for bright field and dark field [24] illumination. To aid in measurement efficiency a 6-degree-of freedom (6-DOF) laser tracker target which inherently generates the frame L^* was fixed to the optical bread board. This was used instead of SMR set $\{SMR_1: SMR_5\}$. A laser tracker capable of 3-degree-of-freedom (3-DOF) point as well as 6-DOF frame measurements was also used. Laser tracker accuracy was better than $20\,\mu m$. Three linear stages having $6\,\mu m$ resolution driven with stepper motors were used to construct the XYZ stage. An assembly constructed from 1.5″ diameter stainless steel optical posts and mounting plate were used to hold measurement samples. The resulting PiCMS is shown in Fig. 11.

3.2. Automatic machine targeting

Automatic targeting of $\mathbf{X}_{obj}$ determines the required motion of the XYZ stage to move the point $\mathbf{X}^*$ to the desired measurement coordinate. For this, triangulation based on the discrepancy

$\boldsymbol{\Delta} = [\Delta X, \ \Delta Y, \ \Delta Z] = \mathbf{X}_{obj} - \mathbf{X}^*$ is used and calculated from the current value of $\mathbf{X}_{obj}$ projected through all three cameras. Using the estimated poses and corresponding camera matricies determined from extrinsic calibration (see Appendix A) gives,

$$\mathbf{x}_{1,obj} = [P_1]\mathbf{X}_{obj} \tag{9}$$

$$\mathbf{x}_{2,obj} = [P_2]\mathbf{X}_{obj} \tag{10}$$

$$\mathbf{x}_{3,obj} = [P_3]\mathbf{X}_{obj} \tag{11}$$

From the extrinsic calibration, the machine coordinate system M was defined with the origin at the Pixel Probe, so that $\mathbf{X}^* = [0,0,0]^T$ and thus the discrepancy is simply $\boldsymbol{\Delta} = \mathbf{X}_{obj}$ so that,

$$\begin{bmatrix} \Delta X \\ \Delta Y \\ \Delta Z \end{bmatrix} = \mathbf{X}_{obj} \tag{12}$$

Accurate targeting is thus achieved by finding $\mathbf{X}_{obj}$. Using the fact that $\mathbf{x}_j \times \mathbf{x}_j = \mathbf{0}$ gives,

$$\mathbf{0} = \mathbf{x}_{j,obj} \times ([P_j]\mathbf{X}_{obj}) \tag{13}$$

Arranging (9)–(11) in the form of $\mathbf{0} = [A]\mathbf{X}_{obj}$, the non-trivial solution $\mathbf{X}_{obj} \neq \mathbf{0}$ is found through the minimization of $\|[A]\mathbf{X}_{obj}\|$ subject to the constraint $\|\mathbf{X}_{obj}\| = 1$. The singular value decomposition (SVD) of $[A]$ is used to estimate $\mathbf{X}_{obj} = \mathbf{X}_{obj,est}$. Where, per usual convention,

$$[A] = [U][D][V]^T \tag{14}$$

Where $[D]$ is a 4×4 diagonal matrix with the singular values of $[A]$, and $[V]^T$ is a 4×4 orthogonal matrix. With,

$$[V] = \begin{bmatrix} v_{11} & v_{12} & v_{13} & v_{14} \\ v_{21} & v_{22} & v_{23} & v_{24} \\ v_{31} & v_{32} & v_{33} & v_{34} \\ v_{41} & v_{42} & v_{43} & v_{44} \end{bmatrix}. \tag{15}$$

In homogeneous coordinates the solution is given by the last column of $[V]$,

$$\mathbf{X}_{obj} = \boldsymbol{\Delta} = \begin{bmatrix} \Delta X \\ \Delta Y \\ \Delta Z \\ 1 \end{bmatrix} = \begin{bmatrix} v_{14}/v_{44} \\ v_{24}/v_{44} \\ v_{34}/v_{44} \\ 1 \end{bmatrix}. \tag{16}$$

The movement required by the XYZ stage to locate the desired coordinate and make $\mathbf{X}^* = \mathbf{X}_{obj}$ in W is then given by, $\Delta X = v_{14}/v_{44}$, $\Delta Y = v_{24}/v_{44}$, $\Delta Z = v_{34}/v_{44}$. In practice it was found that point-to-point targeting using this method should also be iterated a few times to reduce $\boldsymbol{\Delta}$ to as close to zero as possible, with typical values usually ending up in the range of a few microns.

4. Measurements

Because a user can interact with camera images, coordinates on an object in the scene of the trifocal imager can be specified with the click of a mouse. This is achieved by specifying a target coordinate $\mathbf{X}_{target}$ in the images that the XYZ stage drives the Pixel Probe to, where now $\mathbf{X}_{target} = \boldsymbol{\Delta}$. The chosen $\mathbf{X}_{target}$ results from the mode the Pixel Probe is used in, Direct Mode (Section 2.5.1) or Feature Mode (Section 2.5.2.). An interactive ROI that is manipulated on the computer screen allows the user to easily specify $\mathbf{X}_{target}$. For the measurements presented below two types of ROIs were used: a single point ROI for Direct Mode allowed pointing-and-clicking on a coordinate through the images and, a circular ROI in Feature Mode was used where the edge finding algorithm is implemented.

4.1. 2-D objects

Calibrated optical test targets consisting of shapes patterned from (≈ 200 nm thick) chrome deposited on a glass substrate provided a control measurement set to validate the PiCMS for this proof of concept. Such targets are manufactured to tolerances well below the resolution of the Pixel Probe and are certified as calibration standards making them useful for testing purposes (future work will address higher standard calibrated and intercomparison measurements). Coordinate measurements were acquired to determine dimensions and pose of these shapes as they exist within W. Dimensions were compared to manufacturer stated dimensions and uncertainties.

Three kinds of targets were used: square shapes with dimensions ranging from 0.5 mm × 0.5 mm–10 mm × 10 mm, circle targets with diameters ranging from 0.5 mm to 10 mm, and a square grid of 250 μm diameter dots with 500 μm spacing. Manufacturer stated uncertainties (size, spacing) were ± 2.5 μm for all targets. Direct Mode was used to measure coordinates along the perimeter of the squares and circles. Sixteen and eight coordinates were measured around the squares and circle respectively. The targets were placed in the PiCMS at the "Test Object" location (see Fig. 11). Fig. 13 shows the shape target and corresponding coordinate measurements. Data are shown for the 5 mm and 7 mm squares and circles. Lines and circles where fit to these data sets using commercially available spatial metrology software to determine the shape dimensions.

For the 5 mm square the dimensions were found to be 5.000 mm × 5.017 mm with a mean fit deviation from ideal of $\mu = -0.000$ mm and *RMS* fit error of 0.012 mm. For the 7 mm square the dimensions were found to be 7.015 mm × 7.011 mm with $\mu = -0.006$ mm and *RMS* fit error of 0.013 mm. For the 5 mm circle the diameter was found to be 5.015 mm with $\mu = -0.002$ mm and *RMS* fit error of 0.010 mm. For the 7 mm circle the diameter was found to be 7.018 mm with $\mu = 0.000$ mm and *RMS* fit error of -0.099 mm. Fig. 14 shows the fit deviation from the ideal geometry of all data points acquired for the four shapes. Nearly all deviations lie within the range of ± 25 μm with mean deviations below 10 μm. As mentioned above, since measurements are within a world coordinate system their poses are also measured by the PiCMS. From each shape data set the following poses were determined in fixed angle convention $[\theta_x, \theta_y, \theta_z]$: 5 mm square, [91.0208°, 1.9943°, −27.099°]; 7 mm square, [91.005°, 1.9895°, −26.783°]; 5 mm circle, [90.974°, 1.819°, −28.156°]; 7 mm circle,
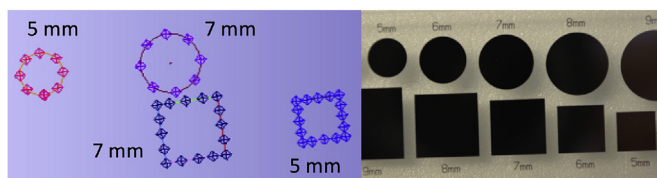

Fig. 13. (Left) Coordinate points measured with the PiCMS for the 5 mm and 7 mm square and circle shapes. (Right) Optical shape target.
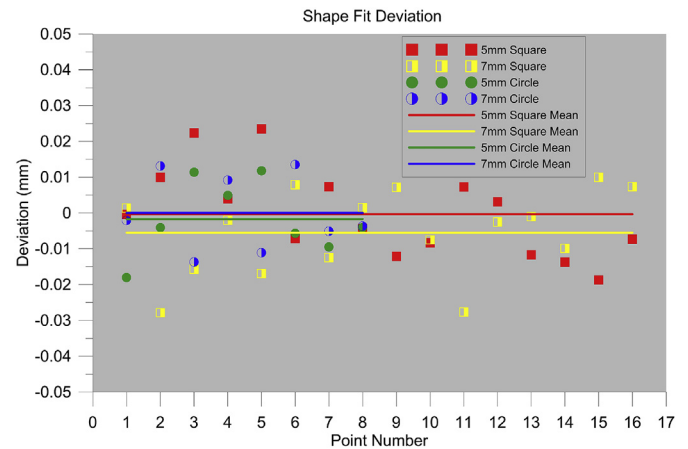

Fig. 14. Plot of the fit deviation of each measurement coordinate from the ideal square and circle shape. Mean fit deviation for each shape is also given (solid lines).

[91.076°, 2.000°, −28.285°]. All poses are nearly identical as they should be since the shapes are patterned on the same glass substrate and thus lie in the same plane.

The dot grid target and corresponding measurement locations are shown in Fig. 15. Feature Mode with an annular ROI was used to find the center of each dot. The center-to-center spacing between the dots in a 5 × 5 sub-grid section spanning a 2 mm × 2 mm patch was measured. The distance between all pairs of dots along the orthogonal directions were calculated for all four separation categories: 0.5 mm, 1.0 mm, 1.5 mm, 2.0 mm resulting in 100 data points. A histogram for these data is shown in Fig. 16 along with the mean and standard deviation (μ, σ) for each dot spacing category, both of which show errors below 20 μm. Tight clustering about each spacing for the data points is clear from the histogram. For comparison, these dots are ≈ 150 times smaller than a typical 38.1 mm diameter SMR laser tracker target yet easily resolved and individually measured in the laser tracker world frame W via the PiCMS.

4.2. 3-D objects

A WR-08 UG-387 microwave waveguide flange was chosen to demonstrate measuring and reconstructing real-world 3-D objects using the PiCMS. The major dimensions of this flange must meet military specification and are standardized to MIL-DTL-3922 [25] with mechanical features ranging across the macro/meso scale. Fig. 17 shows a photo of the WR-08 UG-387 flange.

The ring light (see Fig. 11) was configured for dark-field illumination so as to accentuate edges. The resulting dark-field image with the Pixel Probe at a corner of the WR-08 waveguide opening is also shown in Fig. 17. Again the Pixel Probe has been exaggerated so it is visible in the figure. The PiCMS was used in Direct Mode to measure coordinates along contours of major features. The 3-D reconstruction was generated by fitting geometries (rectangles, circles, cylinders, etc.) to these data using commercially available spatial metrology software provided with the laser tracker. The measured coordinate points and 3-D reconstruction are shown in Fig. 18 along with labeled dimensions. Table 1 compares the dimensions resulting from the 3-D reconstruction to the typically specified dimensions.

The military standardized dimensions are those with tolerances and are listed in bold font. Results show good agreement with designed values. Of the major dimensions **OD1**, **H**, and **W** show the largest discrepancies around 100 μm. In the case of **OD1** this may be due to the chamfer and rounding of the outer surface of the flange which is visible in Fig. 17. In the case of the inner waveguide dimensions **H** and **W** this may be due to the electro-forming process by which the center

Fig. 15. Grid target. (Left) Closeup shows the measurement of the center of one 250 μm diameter dot in the grid. The cluster of edge points are shown in red. The machine co-ordinate system *M* denoted by "Local C.S." with center defining the Pixel Probe is centered on the dot because the coincidence relation is being satisfied. (Center) Acquired data points for the 5 × 5 sub grid. (Right) Dot grid. (For interpretation of the references to color in this figure legend, the reader is referred to the Web version of this article.)
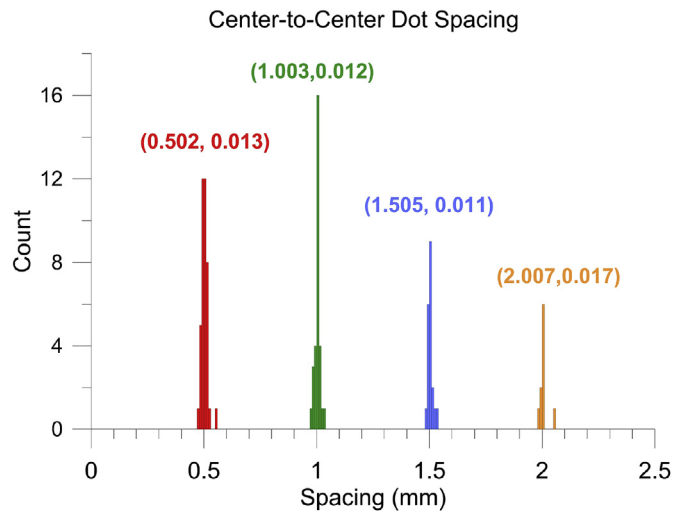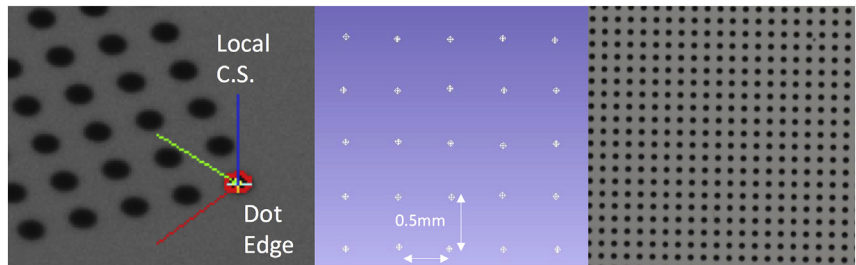

Fig. 16. Histogram for all 100 data points showing tight clustering around each spacing category: 0.5 mm, 1.0 mm, 1.5 mm, 2.0 mm. The mean and standard deviation (μ, σ) is given above each cluster.
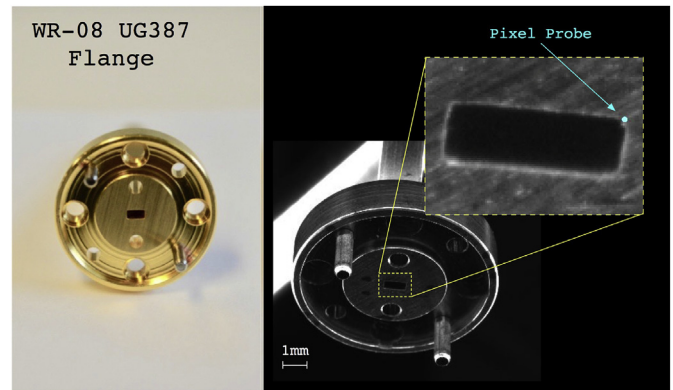

Fig. 17. (Left) The WR-08 UG-387 microwave waveguide flange. (Right) Dark-field image of flange. (Inset) The WR-08 waveguide aperture with Pixel Probe at upper right corner.

rectangular hole is made. In this process a machined madril is first made on which copper is then grown through electrolysis, then the madril dissolved. As can be seen in Fig. 17 the rectangular opening has irregularities in the range of a few pixels (~100 μm) making for rounded corners and non-parallel sides. However, further investigation is needed to asses the source of these discrepancies. Future work will focus on assessing uncertainties that could impact such results. The other major dimensions: (bolt circle) **BC**, secondary alignment pin hole separation **D** and the angular spacing between holes **a** and **b** show differences well within specified tolerances. As these features result from computer numerical control machining and not the electro-forming process, these would be expected to have tighter tolerances.
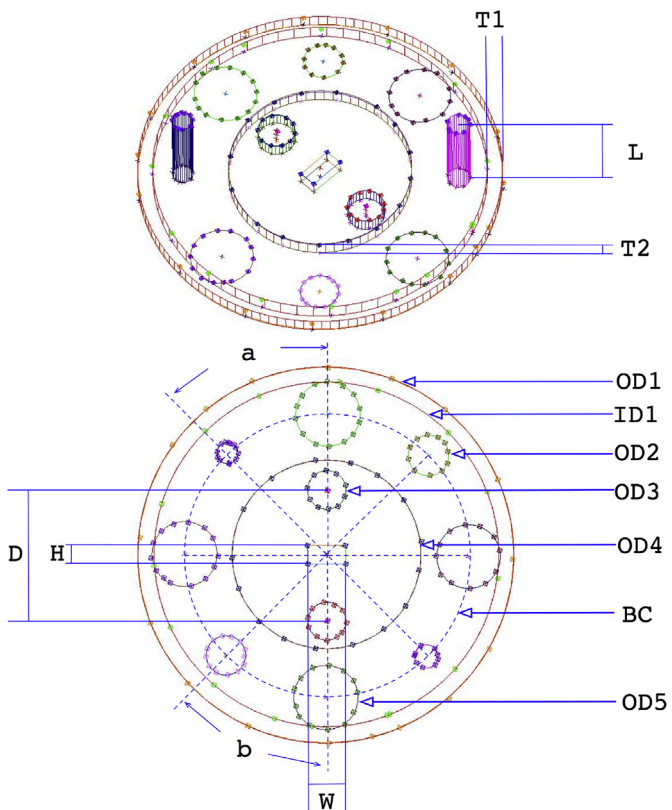

Fig. 18. 3-D reconstruction of the WR-08 UG-387 flange. (top) Out-of-plane and (bottom) in-plane plane views are shown. Locations of the individual co-ordinate measurements are represented as points along with the geometries fitted to them. Dimension labels are shown with corresponding values listed in Table 1.

Table 1
WR-08 UG387 Flange Measurements (units mm unless noted).

Dimension	PiCMS	Typ	Diff	Tol.
OD1	**18.915**	**19.02**	**0.105**	**± 0.0254**
OD2	2.016	2.082	0.067	–
OD3	1.924	1.981	0.057	–
OD4	9.50	9.50	0.00	–
OD5	3.24	3.20	0.04	–
ID1	17.339	17.320	0.020	–
BC	**14.288**	**14.288**	**0.00**	**± 0.0254**
H	**0.926**	**1.016**	**0.091**	**± 0.0254**
W	**1.908**	**2.032**	**0.124**	**± 0.0254**
D	**6.599**	**6.604**	**0.005**	**± 0.0254**
L	5.066	5.00	0.066	–
T1	0.787	0.765	0.022	–
T2	0.743	0.765	0.022	–
a°	**45.114**	**45.0**	**0.114**	**± 0.5**
b°	**44.944**	**45.0**	**0.056**	**± 0.5°**

5. Discussion

The work presented serves as a proof of concept of the PiCMS. One of the strengths of the embodiment used here is the ability to directly measure sub-millimeter objects and edges with a laser tracker. The measurements presented were taken at the edges of samples or on surfaces that had noticeable features. However, on uniform featureless objects this would challenge the current configuration. This suggests the effect of different lighting schemes warrants further investigation.

The simplicity of this system lends well to scaling. The rather modest 5 mega pixel CMOS cameras used here can be easily improved upon as even 50 mega pixel cameras are now readily available. Along with straight forward scaling of the optics this can improve the PiCMS resolution to $\ll 20\,\mu$m while reducing the size of the system considerably.

Because the Pixel Probe is linked directly to the laser tracker and targeting is accomplished via the XYZ stage, the laser tracker can be taken in and out of the system without lose of calibration. Also variations on the PiCMS that do not use a laser tracker can be realized. If relative measurements (not existing within a world frame) are only of interest, the PiCMS can be operated without a laser tracker with some modification. This may be accomplished by relying on the machine coordinate M for determining the location of $\mathbf{X}^*$. In the construction used here the position of encoders on the axes of the XYZ stage would then provide the values used to obtain relative measurements instead of the laser tracker. The accuracy of this method would depend on how well the XYZ stage movement is calibrated to the machine coordinate system. Using the laser tracker as was done here relaxes the calibration requirement of the XYZ stage.

Future and on-going work will also be focused beyond this proof of concept and aim to establish uncertainties and traceability of measurements made with the PiCMS. This includes intercomparison measurements with systems such as the M48 CMM at the National Institute of Standards and Technology.

6. Conclusion

We have presented a type of non-contact coordinate measuring system, the PiCMS, that uses a Pixel Probe instead of a contact probe or stylus for making measurements. This system in essence produces an invisible stylus non-contact probe through the scaled orthographic projection of a spherical mounted reflector by a trifocal imaging system. The Pixel Probe by itself can be used to make measurements, however its usability and convenience is enhanced through the PiCMS configuration. The PiCMS is created through the union of a Pixel Probe, laser tracker and calibrated XYZ stage. The laser tracker provides a means for determining the Pixel Probe World location in 3-D and the XYZ stage allows a user to efficiently target and position the probe on a coordinate to be measured.

A theoretical model for the Pixel Probe and PiCMS is given using multi-view geometry vision theory. Practical elements needed to make the system are given as well as a detailed description of the calibration process needed to actualize it. Measurement results are presented for 2-D calibration grade optical test targets and real world 3-D objects. Measurements demonstrate that in the current configuration accuracy of $< 20\,\mu$m is possible with the PiCMS. Furthermore, in the current configuration the $\approx 20\,\mu$m spatial scale of the Pixel Probe allows for metrology from the macroscale down to the meso/microscale thus extending the dimensional scale of objects a laser tracker alone can measure.

Appendix A. Extrinsic Calibration

Extrinsic calibration of the PiCMS involves establishing the frame-to-frame relationships between M and cameras. Here we use a 3-D-point correspondence method to solve for the individual camera poses $[R_j | \mathbf{t}_j]$ within M. Laser tracker measurements are used for this and for also defining the machine coordinate system M such that the Pixel Probe point $\mathbf{X}^*$ is at the origin. The result are robust estimates of the camera matricies $[P_j]$ which then allow automatic targeting of object coordinate $\mathbf{X}_{obj}$ and for calculating the offset $\mathbf{\Delta} = \mathbf{X}_{obj} - \mathbf{X}^*$. From this the XYZ stage can move autonomously to the measurement location.

For this a set of three dimensional data points are obtained within M (IR^3). This set is denoted by the vector $\mathbf{U}$, with the corresponding set of image points (IR^2) in the j'th camera denoted by the vector $\mathbf{u}_j$,

$$\mathbf{U} = [X_1, Y_1, Z_1, X_2, Y_2, Z_2, ... X_N, Y_N, Z_N]^T, \tag{A.1}$$

$$\mathbf{u}_j = [x_{j1}, y_{j1}, x_{j2}, y_{j2}, ... x_{jN}, y_{jN}]^T, \tag{A.2}$$

where the correspondence between $\mathbf{U}$ and $\mathbf{u}_j$ are related for each set $\{1: N\}$ through the camera projection matrix $[P_j]$ via,

$$\mathbf{u}_j = [P_j] \mathbf{U} = [K_j][R_j | \mathbf{t}_j] \mathbf{U} \tag{A.3}$$

The pose of each camera within M is then estimated from this correspondence.

Appendix A.1 Process

$\mathbf{X}^*$ of the Pixel Probe is taken as the origin of the machine coordinate M and the XYZ stage is set with all three axes at the midpoint of travel so as to maximize available movement. A point target that is visible from all three cameras is fixed in place which is used to define the set of points $\mathbf{U}$ and image points $\mathbf{u}_j$. For this proof of concept, the end of a thin wire with a diameter under 50 μm was used as the point target. The wire was held securely in place with a small clamp such that it is observed in the field of view of all three cameras. The end of the wire acts as the object coordinate $\mathbf{X}_{wire} = \mathbf{X}_{obj}$.

With the XYZ stage at the middle of travel, the end of the wire is positioned to coincide with the Pixel Probe such that, $\mathbf{X}_{wire} = \mathbf{X}^*$ and $\Delta = 0$. The XYZ stage is then moved to several locations along the $\pm$ X, $\pm$ Y, $\pm$ Z directions. At each location of the stage, the pixel coordinates of the end of the wire $\mathbf{x}_{j,wire} = [x_{j,wire}, y_{j,wire}]^T$ in each camera image are identified and recorded creating a set of *known* image points. We define the vectors which contain these known image points for all three cameras as $\mathbf{u}_{1,0}, \mathbf{u}_{2,0}, \mathbf{u}_{3,0}$. At the same time the location of the Pixel Probe measured by the laser tracker in M is recorded. The axes of M are defined by moving the XYZ stage in the $\pm$ X, then $\pm$ Y, then $\pm$ Z directions independently. The laser tracker data were then shifted so that the starting point of the XYZ stage, where $\mathbf{X}_{wire} = \mathbf{X}^*$, defined the machine origin $M(0,0,0)$. These data were

then used to estimate the camera poses $[R_j|\mathbf{t}_j]$.

Appendix A.2Pose Estimation

As the three cameras are fixed relative to one another, a linear least squares algorithm based on Newtonian iteration was used to estimate the camera poses. Although more complex minimization techniques could be used for pose estimation, this method is relatively straight forward to implement and is successful for this purpose. Expanding $[R_j|\mathbf{t}_j]$ the rotation matrix is,

$$[R_j(\theta_{jx}, \theta_{jy}, \theta_{jz})] = [R_{jz}][R_{jy}][R_{jx}] \tag{A.4}$$

where using a fixed angle convention,

$$[R_{jx}] = \begin{bmatrix} 1 & 0 & 0 \\ 0 & cos(\theta_{jx}) & -sin(\theta_{jx}) \\ 0 & sin(\theta_{jx}) & cos(\theta_{jx}) \end{bmatrix} \tag{A.5}$$

$$[R_{jy}] = \begin{bmatrix} cos(\theta_{jy}) & 0 & sin(\theta_{jy}) \\ 0 & 1 & 0 \\ -sin(\theta_{jy}) & 0 & cos(\theta_{jy}) \end{bmatrix} \tag{A.6}$$

$$[R_{jz}] = \begin{bmatrix} cos(\theta_{jz}) & -sin(\theta_{jz}) & 0 \\ sin(\theta_{jz}) & cos(\theta_{jz}) & 0 \\ 0 & 0 & 1 \end{bmatrix} \tag{A.7}$$

with the translation column vector,

$$\mathbf{t}_j = [t_{jx}, t_{jy}, t_{jz}]^T \tag{A.8}$$

The coordinates of the image points $\mathbf{u}_j$ which result from the projection of $\mathbf{U}$ by camera C_j, are dictated by the pose variables θ_x, θ_y, θ_z, t_{jx}, t_{jy}, t_{jz}. Defining a pose vector $\mathbf{v}_j$ as,

$$\mathbf{v}_j = [\theta_{jx}, \theta_{jy}, \theta_{jz}, t_{jx}, t_{jy}, t_{jz}]^T \tag{A.9}$$

and

$$\partial\mathbf{v}_j = [\partial\theta_{jx}, \partial\theta_{jy}, \partial\theta_{jz}, \partial t_{jx}, \partial t_{jy}, \partial t_{jz}]^T \tag{A.10}$$

we write the projection matrix as,

$$[P_j] = [K_j][R_j|\mathbf{t}_j] = [K_j][H(\mathbf{v}_j)] \tag{A.11}$$

giving,

$$\mathbf{u}(\mathbf{v}_j)_j = [K_j][H(\mathbf{v}_j)]\mathbf{U} \tag{A.12}$$

Furthermore, given the known image point coordinates $\mathbf{u}_{j,0}$ from above we define the cost function,

$$|\mathbf{u}(\mathbf{v}_{j,est})_j - \mathbf{u}_{j,0}|^2 = r_j \tag{A.13}$$

In estimating the poses, we wish to find $\mathbf{v}_j = \mathbf{v}_{j,est}$ which minimizes the residual r_j. An initial estimate of the pose, $\mathbf{v}_{j,int}$ is iteratively perturbed based on the value of r_j. The pose $\mathbf{v}_j$ and image points $\mathbf{u}_j$ are related through the Jacobian matrix given by,

$$[\mathbf{J}] = \left[\frac{\partial\mathbf{u}_j}{\partial\mathbf{v}_j}\right] = \begin{bmatrix} \frac{\partial u_{j1}}{\partial v_1} & \frac{\partial u_{j1}}{\partial v_2} & \frac{\partial u_{j1}}{\partial v_3} & \cdots & \frac{\partial u_{j1}}{\partial v_6} \\ \frac{\partial u_{j2}}{\partial v_1} & \frac{\partial u_{j2}}{\partial v_2} & \frac{\partial u_{j2}}{\partial v_3} & \cdots & \frac{\partial u_{j2}}{\partial v_6} \\ \vdots & \vdots & \vdots & \cdots & \vdots \\ \frac{\partial u_{jN}}{\partial v_1} & \frac{\partial u_{jN}}{\partial v_2} & \frac{\partial u_{jN}}{\partial v_3} & \cdots & \frac{\partial u_{jN}}{\partial v_6} \end{bmatrix} \tag{A.14}$$

Which is approximated as,

$$[\mathbf{J}] = \left[\frac{\partial\mathbf{u}_j}{\partial\mathbf{v}_j}\right] \approx \frac{\mathbf{u}_j(\mathbf{v}'_j + \varepsilon_j) - \mathbf{u}_j(\mathbf{v}'_j)}{\varepsilon_j} \tag{A.15}$$

where ε_j is a small number used to calculate the derivatives and $\mathbf{v}'_j$ is the *current* pose at any iteration. The change in the pose needed to reduce r_j is computed by,

$$\partial\mathbf{u}_j = [\mathbf{J}]\partial\mathbf{v}_j \tag{A.16}$$

$$\partial\mathbf{v}_j = [J^{-1}]\partial\mathbf{u}_j \tag{A.17}$$

where $[J^{-1}]$ is the pseudo-inverse defined in the usual fashion as,

$$[J^{-1}] = ([\mathbf{J}]^T[\mathbf{J}])^{-1}[\mathbf{J}]^T \tag{A.18}$$

Letting, $\partial\mathbf{u}_j = \mathbf{u}_{j,0} - \mathbf{u}_j(\mathbf{v}'_j)$ We have,

$$\mathbf{v}_j^{''} = \mathbf{v}_j^{'} + \partial \mathbf{v}_j = \mathbf{v}_j^{'} + ([\mathbf{J}]^T [\mathbf{J}])^{-1} [\mathbf{J}]^T (\mathbf{u}_{j,0} - \mathbf{u}_j(\mathbf{v}_j^{'})) \tag{A.19}$$

where $\mathbf{v}_j^{''}$ is the updated pose. The $\mathbf{u}_j$ as well as the derivatives in $[\mathbf{J}]$ are updated for each new $\partial \mathbf{v}$. The process is continued and r_j and $\partial \mathbf{u}_j = \mathbf{u}_{j,0} - \mathbf{u}_j(\mathbf{v}_j^{'})$ recalculated for each iteration until the desired accuracy (value of r_j) is achieved. The final value of the pose is then taken as the estimate, $\mathbf{v}_{j,est} = \mathbf{v}_{j,final}^{'}$. From the estimated pose vectors $\mathbf{v}_{1,est}$, $\mathbf{v}_{2,est}$, $\mathbf{v}_{3,est}$ the camera projection matricies can then be calculated as,

$$[P_1] = [K_1][H(\mathbf{v}_{1,est})] \tag{A.20}$$

$$[P_2] = [K_2][H(\mathbf{v}_{2,est})] \tag{A.21}$$

$$[P_3] = [K_3][H(\mathbf{v}_{3,est})] \tag{A.22}$$

References

[1] Hocken JR, Pereira PH. Coordinate measuring machines and systems. second ed. CRC Press; 2016.

[2] Hocken RJ, Borchardt BR. On characterizing measuring machine geometry. NBSIR 1979:79–1752.

[3] Stoup JR, Doiron TD. Accuracy and versatility of the NIST M48 coordinate measuring machine. Proc SPIE 2001;4401:136–46.

[4] Cuypers W, Gestel NV, Voet A, Kruth JP, Mingneau J, Bleys P. Optical measurement techniques for mobile and large-scale dimensional metrology. Optic Laser Eng 2009;47:292–300.

[5] Bqersad J, Poozesh P, Niezrecki C, Avitabile P. Photogrammetry and optical methods in structural dynamic-A review. Mech Syst Signal Process 2017;86:17–34.

[6] Chan FMM, Davis EJ, King TG, Stout KJ. Some performance characteristics of multi-axis touch trigger probe. Meas Sci Technol 1997;8:837–48.

[7] Petz N, Tutsch R, Christoph R, Matthias A, Hopp B. Tactile Probes for three dimensional microparts. J Meas 2012;45:2288–98.

[8] Herman G, Santha G. Construction of tactile measuring probes for coordinate measurements. Procedia Mater Sci 2014;5:1519–27.

[9] Bos EJC. Aspects of tactile probing on the micro scale. Precis Eng 2011;35:228–40.

[10] Gestel VN, Cuypers S, Bleys P, Kruth JP. A performance evaluation test for laser line scanner as on CMMs. Optic Laser Eng 2009;47:336–42.

[11] Mohammed A, Ismail L. Design and analysis of a 3D laser scanner. J Meas 2017;111:122–33.

[12] Valkenburg RJ, McIvor AM. Accurate 3D measurement using a structured light system. Image Vis Comput 1998;16:99–110.

[13] Muralikrishnan B, Phillips S, Sawyer D. Laser trackers for large-scale dimensional metrology: a review. J Prec Eng 2016;44:13–28.

[14] Performance evaluation of laser-based spherical coordinate measurement systems. ASME B89.4.19-2006.

[15] Estler WT, Edmundson KL, Peggs GN, Parker DH. Large-scale metrology-an update. CIRP Annals 2002;51:587–609.

[16] Gordon JA, Novotny DR. A single pixel touchless laser tracker probe. J CMSC 2015;10:1221.

[17] Gordon JA, Borenstein SS. Freezing time: dynamic laser tracker measurements with the pixel probe using temporal aliasing. J CMSC 2016;11:4–10.

[18] Hartley R, Zisserman A. Multiple view geometry in computer vision. second ed. 2003. Cambridge UK.

[19] Jain VK. Micromanufacturing process. C.R.C Press; 2012.

[20] Greivenkamp JE. Field guide to geometrical optics. SPIE press; 2004.

[21] Snyder JP. Map projections-A working manual vol. 1395. U.S.G.S. Professional Paper; 1985. p. 145–53.

[22] Palmer JM, Grant BG. The art of radiometry. SPIE press; 2009.

[23] Smith WJ. Modern optical engineering. third ed. McGraw Hill; 2000.

[24] Sanz JLC, Merkle F, Wong KY. Automated digital visual inspection with dark-field microscopy. J Opt Soc Am A 1985;2:1857–62.

[25] Michael B. Rectangular waveguide flange nomenclature (correspondence). IEEE Trans Microw Theor Tech 1965;13:469471.